Modeling the thermal shock induced cracking in ceramics

Luiz Felipe Faria Ricardo, Dominique Leguillon, Guillaume Parry, Aurélien Doitrand

Modelling the thermal shock induced cracking in ceramics

Luiz Felipe Faria Ricardo[a], Dominique Leguillon[b], Guillaume Parry[a], Aurelien Doitrand[c,*]

[a] *Université Grenoble-Alpes - CNRS UMR 5266, SIMaP, F-38000 Grenoble, France*
[b] *Institut Jean le Rond d'Alembert, Sorbonne Universités, CNRS, UMR 7190, Paris, France*
[c] *Université Lyon, INSA-Lyon, MATEIS UMR CNRS 5510, F-69621 Villeurbanne Cedex, France*

Abstract

Prediction of surface cracking in ceramics due to quenching is performed numerically using either the coupled criterion or a cohesive zone model. Under such a thermal shock, a network of short cracks with minimal spacing between them initiate and propagate until some of them stop while the others continue propagating. The numerical implementation consists of a periodic array of cracks modeled by a representative volume element. It allows crack initiation, simultaneous propagation and period doubling to be predicted. The investigation of the crack period doubling allows a precise determination of the optimal crack spacing, which decreases with an increasing thermal shock amplitude. The predicted crack spacing results are in agreement with experimental measurements.

Keywords: Quenching; Thermal shock; Coupled criterion; Cohesive zone

1. Introduction

Industrial ceramics are known for their low coefficient of thermal expansion (CTE) which gives them high thermal stability, hence their use in thermal engines and in the aeronautics and aerospace industry. However, it is observed that surface cracking, an undesired phenomenon, occurs when they are sharply cooled down [3]. Usually, in a metal, quenching triggers a brutal shrinkage of the surface which deforms plastically. When cooling down goes on, the core of the material in turn shrinks, putting the surface under compression and leading to a strengthening effect. Unfortunately, being brittle, ceramics cannot deform plastically, so if the surface shrinkage is too large, cracks will appear in order to accommodate the deformation. To have experimental evidence of this phenomenon, quenching experiments have been conducted by various authors on ceramic bars (Al_2O_3) using a specific setup [13, 25, 26, 32] (see Fig. 1).

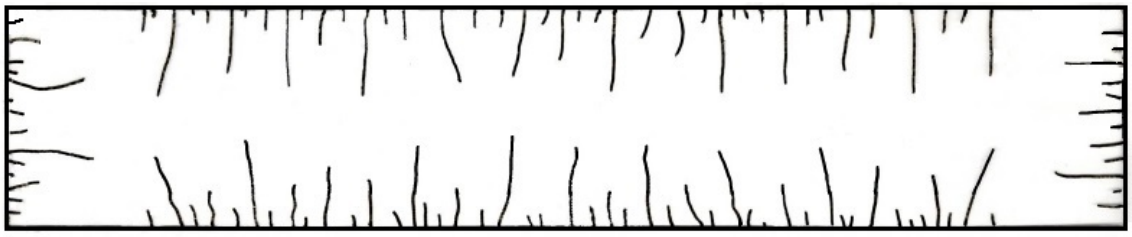

Figure 1: One side of a specimen after a thermal shock about 400 K (reprinted from [13]).

The thermal shock caused by a sudden cooling plays an important role in the fracture pattern. Indeed, in case of a slow cooling or drying process of a thin film on a rigid substrate which prevents effective shrinkage, a first group of cracks is formed with a given (rather large) spacing and new cracks are continually added as the cooling or drying process goes on, ultimately leading to saturation [11, 15, 17, 18]. On the contrary, when cooling down is sudden, it seems that a set of cracks with minimal spacing appears. These cracks are constrained to grow with the minimal spacing until an instability takes place leading to several successive period doubling events [3, 11, 12].

*Corresponding author
Email address: aurelien.doitrand@insa-lyon.fr (Aurelien Doitrand)

The numerical simulation of such a phenomenon has proved difficult to carry out. In parallel with the simple model proposed by Bahr [3] other approaches have emerged. Jenkins [11, 12] and Jiang et al. [13] used a method based on finite elements (FE) computations and an energy minimization principle to predict crack spacing. To this aim Li et al. [21] proposed a convincing, but not so easy to implement, method relying on a non-local damage model. More recently a phase field approach was developed [5, 28]. In this latter approach, a thin layer of homogeneously damaged material first appears on the surface before an instability takes place leading to the formation of a first periodic network of close cracks. The subsequent study of the growth of these cracks, which is allowed by the phase field method, describes the instabilities leading to period doubling.

The phenomenon of multi-cracking resulting of surface shrinking is in its first stage more akin to a crack initiation problem than to a crack growth. The traditional tools of brittle fracture mechanics are therefore ineffective. Specific models must be used, two of them are proposed hereafter. The coupled criterion (CC) combines an energy and a stress condition [14, 31] and the cohesive zone model (CZM) relies on a traction-separation relationship across fracture surfaces [24]. They allow determining, for a given temperature drop ΔT and a given crack spacing d:

1) crack initiation time and length,

2) crack period doubling point time and length,

3) crack length variation as a function of time.

Note that, the further crack growth is either simulated using the classical Griffith criterion or by using the cohesive zone model beyond the crack initiation stage.

It can be pointed out that the proposed model allows varying the crack spacing d which is not known *a priori*. A method aiming at determining the optimal crack spacing is presented in the following. In both approaches, the repeated crack pattern is described using a periodicity assumption. The width of the spacial period corresponds to the crack spacing.

2. The thermal conduction problem

To model the surface cracking phenomenon occurring due to surface shrinking in the very early times following the thermal shock and solve it numerically, it is important to have a sufficiently refined thermal conduction model, especially with regard to boundary conditions. It is briefly recalled below.

We consider the 2D problem of an infinitely long along Ox specimen with width $2w$ so that the heat equation is a 1D equation in Oy direction. The specimen is symmetric with respect to the Ox axis, T, t and y respectively denotes the temperature, time and space variable.

The heat equation writes:

$$\rho \frac{\partial T}{\partial t} = a \frac{\partial^2 T}{\partial y^2} \tag{1}$$

where $a = \frac{k}{\rho c_p}$ ($\mathrm{m^2\ s^{-1}}$) is the diffusivity coefficient, k ($\mathrm{W\ m^{-1}\ kg^{-1}}$) the thermal conductivity, ρ ($\mathrm{kgm^{-3}}$) the density and c_p ($\mathrm{J\ kg^{-1}\ K^{-1}}$) the specificic heat capacity. We define the dimensionless reduced time $\overline{t}$, space variable $\overline{y}$ and temperature $\overline{T}$ as:

$$\overline{t} = \frac{at}{w^2}\ ;\ \overline{y} = \frac{y}{w}\ ;\ \overline{T} = \frac{T - T_0}{T_{\mathrm{ext}} - T_0} \tag{2}$$

where T_0 is the initial temperature in the specimen and T_{ext} is the outer temperature. In the present case of a thermal shock leading to shrinking and cracking $T_0 >> T_{\mathrm{ext}}$. As a consequence, Eqn. (1) rewrites:

$$\frac{\partial \overline{T}}{\partial \overline{t}} = \frac{\partial^2 \overline{T}}{\partial \overline{y}^2} \tag{3}$$

The Fourier condition on the bottom face of the specimen ($y = -w$) is :

$$k \frac{\partial T(-w,t)}{\partial y} = -h(T(-w,t) - T_{ext}) \tag{4}$$

where h (W m^2 K^{-1}) is the convective heat transfer coefficient. Introducing the dimensionless Biot number $B = \frac{hw}{k}$, Eqn. (4) becomes:

$$\frac{\partial \overline{T}(-1,\bar{t})}{\partial \overline{y}} = -B\overline{T}(-1,\bar{t}) \tag{5}$$

In addition the symmetry condition along the (Ox) axis is

$$\frac{\partial T}{\partial y} = 0 \; i.e. \; \frac{\partial \overline{T}}{\partial \overline{y}} = 0 \tag{6}$$

The solution to this system is [7]:

$$\overline{T}(\overline{y},\bar{t}) = \sum_{i>0} A_i exp(-c_i^2 \bar{t}) cos(c_i \overline{y}) - 1 \tag{7}$$

with

$$A_i = \frac{2sin(c_i)}{c_i + sin(c_i)cos(c_i)} \tag{8}$$

where the c_i's are solutions to the transcendent equation:

$$c_i sin(c_i) - Bcos(c_i) = 0 \tag{9}$$

In the sequel, for simplicity, the material coefficients are assumed to be independent of the temperature although this is only an approximation [13]. The temperature variation in time and space is modeled by implementation of the solution (7) to the heat equation in a user subroutine with 30 terms. Results are illustrated in Figure 2. Small oscillations can be seen in Figure 2b for $\bar{t} = 0.0005$ due to the limited number of terms used in (7).

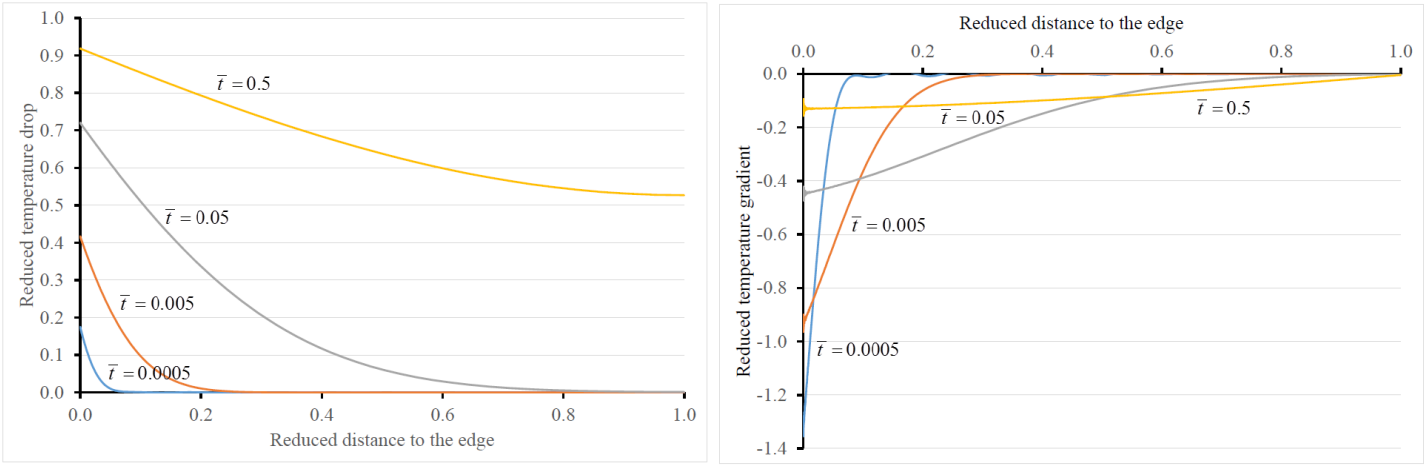

Figure 2: Reduced temperature (a) drop $\bar{T}$ and (b) gradient as a function of the reduced distance to the edge at different reduced time $\bar{t}$.

It must be pointed out that the above equations and solution remain unchanged if cracks develop parallel to the $0y$ axis, since there is no thermal exchange in the Ox direction.

3. The coupled criterion to predict crack nucleation

The CC combines an energy and a stress condition. This approach is particularly well suited to simulate the initiation of new cracks at stress concentration points in brittle materials, such as ceramics [16, 19, 22].

3.1. The criterion

The CC extends in a way the Griffith criterion and allows to predict crack onset at stress concentration points [31]. It meets two conditions: an energy one, close to the Griffith condition although written in an incremental form instead of a differential one, and a stress condition. It does not question Griffith's criterion, it coincides with it at the tip of a crack and with the maximum tension that a material can undergo (strength) in the absence of stress concentration. The major property that emerges from this criterion is that the initiation of a new crack is sudden with a jump over a given length (often small) before continuing to grow or stop.

Its implementation can be done in two ways: (i) the asymptotic approach, not used here for reasons that will be explained below, assumes that the initial crack jump is small compared to all the dimensions of the studied structure; (ii) the full FE approach which has fewer restrictive conditions but requires a higher numerical effort.

Let us consider an uncracked structure and solve the elastic or thermo-elastic problem using FE. First, the potential energy $W_{\mathrm{P}}(0)$ can be computed as well as the tension $\sigma(s)$ acting on the presupposed crack path (thus prior to crack initiation) emanating from the stress concentration point under consideration (s is the abscissa along the presupposed crack path). Then, if double nodes have been inserted along this presupposed path, each pair can be released step by step to simulate a crack of increasing length l. At each step the corresponding potential energy $W_{\mathrm{P}}(l)$ is computed and the incremental energy condition can be written:

$$-\Delta W_{\mathrm{P}} = W_{\mathrm{P}}(0) - W_{\mathrm{P}}(l) \geq G_{\mathrm{c}} l \;\Rightarrow G_{\mathrm{inc}} \geq G_{\mathrm{c}} \text{ with } G_{\mathrm{inc}} = \frac{W_{\mathrm{P}}(0) - W_{\mathrm{P}}(l)}{l} \tag{10}$$

Where G_{c} is the fracture energy of the material identified with the material toughness through Irwin's relationship. Here G_{inc} is the so-called incremental energy release rate. It differs from the usual definition of the energy release rate G which is of a differential form

$$G = -\frac{\partial W_{\mathrm{P}}}{\partial l} \tag{11}$$

On the other hand, the stress condition states that the tensile stress prior to crack formation must exceed the tensile strength of the material σ_{c} all along the initial crack jump:

$$\sigma(s) \geq \sigma_{\mathrm{c}} \text{ for } 0 \leq s \leq l \tag{12}$$

These two inequalities allow to compute the crack jump l_{c} at initiation and the critical prescribed load triggering the new crack formation.

This full FE approach is adopted for two reasons. First, as observed in the experiments, cracks that appear are close to each other and the spacing is of the same order of magnitude than cracks length, violating the asymptotic assumption that the crack length is far smaller than any other dimension of the structure. Second, in the early times of the quenching the temperature gradient is very large which can lead to the definition of a second small parameter that may interact with the crack length.

3.2. The CC representative volume element

As already mentioned, a large number of cracks initially appear close to one another and it would be extremely cumbersome to model them all. To avoid this problem, calculations are carried out on an elementary volume representative of the entire structure by periodically repeating the pattern. This means that we study the central part of the specimen, far from the ends. The width d of this representative volume element (RVE) is a parameter of the model that will be used to represent the crack spacing (Figure 3, not at the right scale). This approach has already been used successfully in [17, 18].

Because of symmetries, only 1/4 of the RVE (Figure 3) is meshed, its height is 1/2 of the specimen width w. Along the presupposed crack path the mesh size increases upward from 1.7 μm to 8 μm at 0.2 mm from the bottom (it is checked afterward that this is big enough to cover the actual crack length). It then continues to increase to reach 0.2 mm on the upper part.

Due to the symmetry of the specimen with respect to Ox there is no bending, the actual displacement field in the RVE $\underline{U}$ is taken as the superposition of an elementary thermally activated field $\underline{U}^{\mathrm{th}}$ (baptized shrinking in Figure 4) and an elementary mechanical traction $\underline{U}^{\mathrm{el}}$ acting on the left and right faces (stretching in Figure 4):

$$\underline{U}(x,y,t) = \Delta T_0 \; \underline{U}^{\mathrm{th}}(x,y,t) + z \; \underline{U}^{\mathrm{el}}(x,y) \tag{13}$$

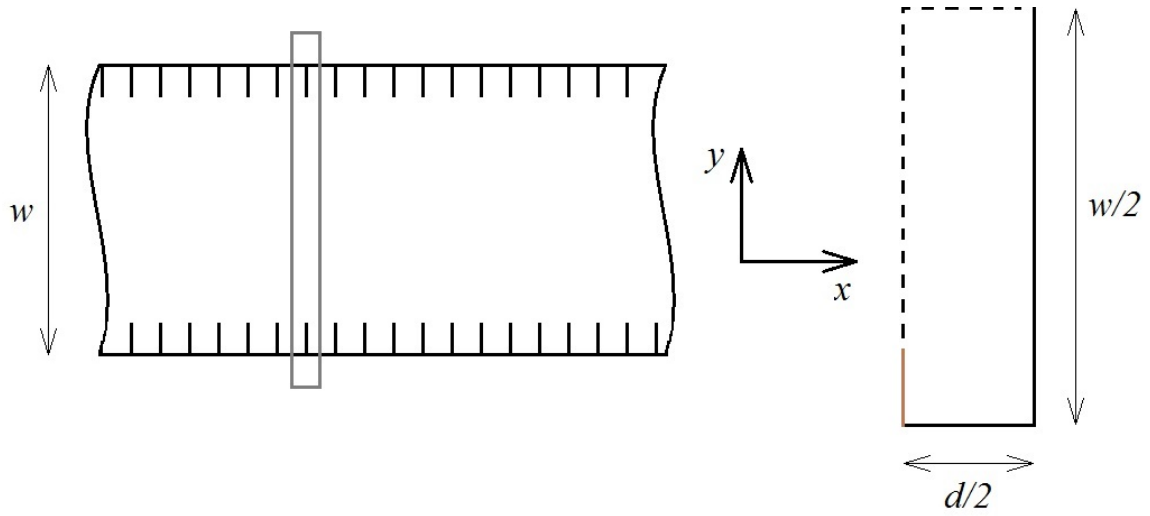

Figure 3: Left: the RVE used to study the simultaneous onset and growth of a periodic set of cracks. Right: 1/4 of the RVE, the dashed lines are symmetry axes, the red solid line at the bottom left is the presupposed crack path.

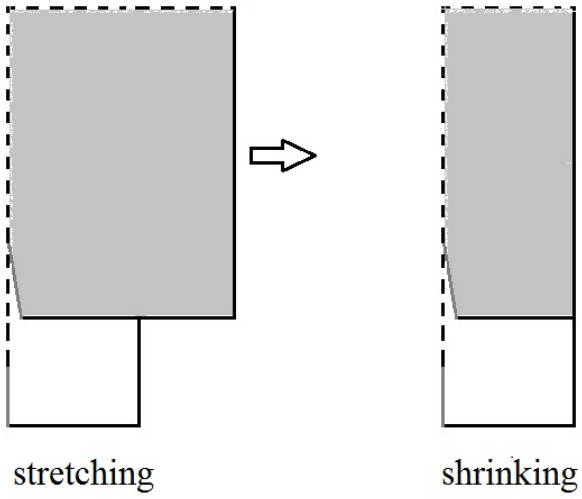

Figure 4: 1/4 RVE stretching due to a unit traction and shrinking due to a unit cooling.

Where $\Delta T_0 = T_{\text{ext}} - T_0$ is the prescribed temperature drop. The unknown weight z, function of t, is linked to the average horizontal strain $\bar{\varepsilon}_{xx}$

$$z = \bar{\varepsilon}_{xx} \frac{d}{2} \tag{14}$$

It is obtained writing that the resultant force $\mathcal{R}(\underline{U})$ acting on the lateral faces of the specimen vanishes

$$\Delta T_0 \ \mathcal{R}(\underline{U}^{\text{th}}) + z \ \mathcal{R}(\underline{U}^{\text{el}}) = 0 \tag{15}$$

The two elementary solutions fulfil the balance equation

$$-\nabla.\underline{\underline{\sigma}}^{\text{th}} = 0; \ \ -\nabla.\underline{\underline{\sigma}}^{\text{el}} = 0 \tag{16}$$

Where the stress tensors $\underline{\underline{\sigma}}^{\text{th}}$ and $\underline{\underline{\sigma}}^{\text{el}}$ are defined by the constitutive equations

$$\underline{\underline{\sigma}}^{\text{th}} = \boldsymbol{C} : \left(\nabla \underline{U}^{\text{th}} - \alpha \boldsymbol{I} \right) \tag{17}$$

and

$$\underline{\underline{\sigma}}^{\mathrm{el}} = \boldsymbol{C} : \nabla \underline{U}^{\mathrm{el}} \tag{18}$$

Here $\boldsymbol{C}$ is the Hooke tensor depending on Young's modulus E and Poisson's ratio ν of the material (isotropy is assumed). In (17), α is the CTE and $\boldsymbol{I}$ the second order identity tensor (isotropy is assumed as well). Eqn. (17) is the thermoelastic constitutive law for a temperature change equal to unity.

The bottom face Γ_{b} of the RVE is traction free

$$\sigma_{xy}^{\mathrm{th}} = \ \sigma_{yy}^{\mathrm{th}} = 0 \ \sigma_{xy}^{\mathrm{el}} = \ \sigma_{yy}^{\mathrm{el}} = 0 \tag{19}$$

Horizontal displacements are prescribed on the left face Γ_{l} of the RVE

$$U_x^{\mathrm{th}} = 0; \ U_x^{\mathrm{el}} = -1 \tag{20}$$

For symmetry reasons calculations are carried out only on 1/4 of the RVE (see Figure 3) and the two elementary solutions fulfil the symmetry conditions along Ox

$$U_y^{\mathrm{th}} = 0; \ \sigma_{xy}^{\mathrm{th}} = 0; \ U_y^{\mathrm{el}} = 0; \ \sigma_{xy}^{\mathrm{el}} = 0 \tag{21}$$

and along Oy

$$U_x^{\mathrm{th}} = 0; \ \sigma_{xy}^{\mathrm{th}} = 0; \ U_x^{\mathrm{el}} = 0; \ \sigma_{xy}^{\mathrm{el}} = 0 \tag{22}$$

Once $\underline{U}^{\mathrm{th}}$ and $\underline{U}^{\mathrm{el}}$ have been numerically computed using FE for various crack length l, the change in potential energy between the uncracked and cracked states can be calculated [18]

$$-\Delta W_{\mathrm{P}} = \frac{1}{2}\Delta T_0^2 \Delta(\boldsymbol{K} X^{\mathrm{th}} X^{\mathrm{th}}) + \Delta T_0 z \Delta(B X^{\mathrm{el}}) - \frac{1}{2} z^2 \Delta(\boldsymbol{K} X^{\mathrm{el}} X^{\mathrm{el}}) \tag{23}$$

Where $\boldsymbol{K}$ is the stiffness matrix that results from the discretization of the two problems (the same in both cases), X^{th} and X^{el} are the nodal vectors solution to the discretized systems and B the vector of nodal forces involved in the thermoelastic problem. Note that in (23) X^{th} and z both depend on t and that this calculation must be carried out at each time step.

Once the cracks have initiated, the further growth can be studied using Griffith's criterion, the derivative being approximated by a difference in potential energy at each step of unbuttoning:

$$-\frac{\partial W_{\mathrm{P}}}{\partial l} \geq G_{\mathrm{c}} \tag{24}$$

It is thus possible to compare from an energetic point of view, on the one hand the simultaneous crack growth using the RVE of Figure 3 and on the other hand the growth of one crack out of two by growing only the left crack in the RVE of Figure 5.

3.3. CC Results

For convenience, although it is a cooling process, the values of $\Delta T_0 = T_{\mathrm{ext}} - T_0$ and $\Delta T = T - T_0$ are noted as positive in the following.

The simulations have been carried out on the Alumina already described in [21]. The material parameters are: Young's modulus $E = 370$ GPa, Poisson's ratio $\nu = 0.3$, tensile strength $\sigma_{\mathrm{c}} = 180$ MPa, fracture energy $G_{\mathrm{c}} = 24.3$ J m^{-2} (toughness $K_{\mathrm{Ic}} = 3.14$ MPa m$^{1/2}$), density $\rho = 3980$ kg m^{-3}, thermal conductivity $k = 31$ W m^{-1} K^{-1}, specific heat capacity $c_p = 880$ J kg^{-1} K^{-1}, convective heat transfer coefficient $h = 5\ 10^4$ W m^{-2} K^{-1} (Biot's number $B \approx 8$).

The way the CC is applied is illustrated in Figures 6, 7 and 8 for $t = 1.6$ ms and a given crack spacing 2 mm. It is written in a dimensionless way so that the two conditions 10 and 12 can be plotted on the same graph. Obviously, in Figure 6 the stress condition holds true for $l \leq 0.06$ mm but the energy condition nowhere. No crack initiation is possible after $t = 1.6$ ms for a temperature drop $\Delta T_0 = 500$ K. Under the same conditions, but with $\Delta T_0 = 550$ K (Figure 7), again no possible crack initiation, the two conditions holds true but on disjointed segments. Initiation can occur for $\Delta T_0 = 600$ K, with $l_{\mathrm{c}} = 0.075$ mm. This length is the initiation length but in general not an arrest length as seen further. Finally, from Figure 9 for $\Delta T_0 = 650$ K, it is clear that it still exists a solution at an earlier time than $t = 1.6$ ms.

The elapsed time before crack nucleation depends on the temperature drop as shown in Figure 10. Moreover, for temperature drops smaller than $\Delta T_0 = \Delta T_{\mathrm{min}} = 120$ K no crack nucleation is predicted.

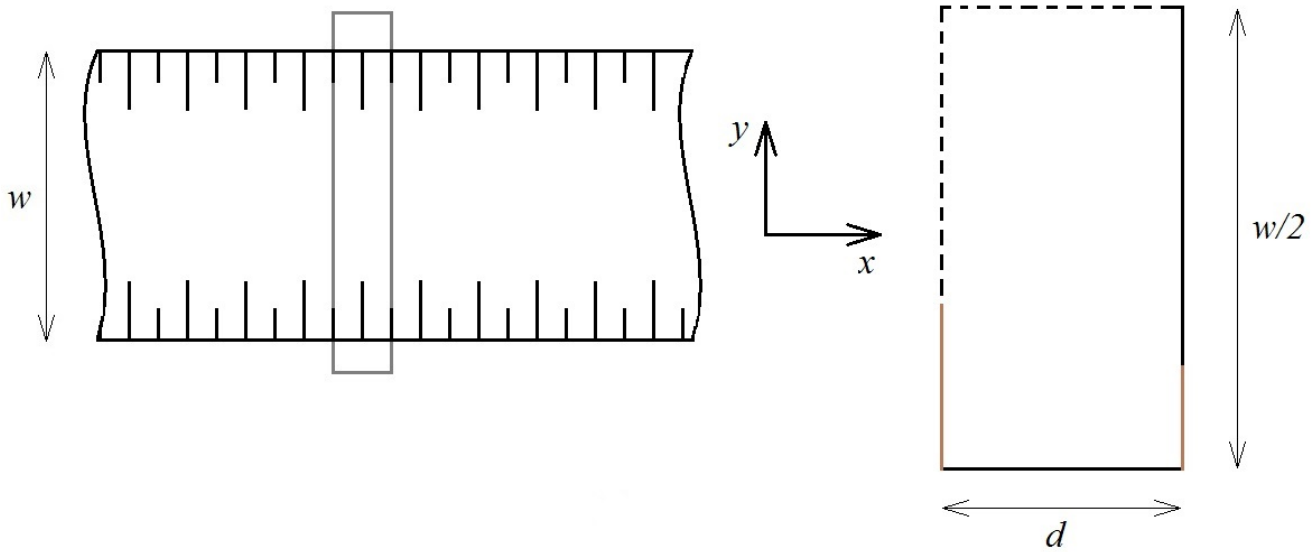

Figure 5: Left: the RVE used to study a possible doubling of the period. Right: 1/4 of the RVE, the dashed lines are symmetry axes, the red solid line at the bottom left is the growing crack and the one at the bottom right is an arrested one.

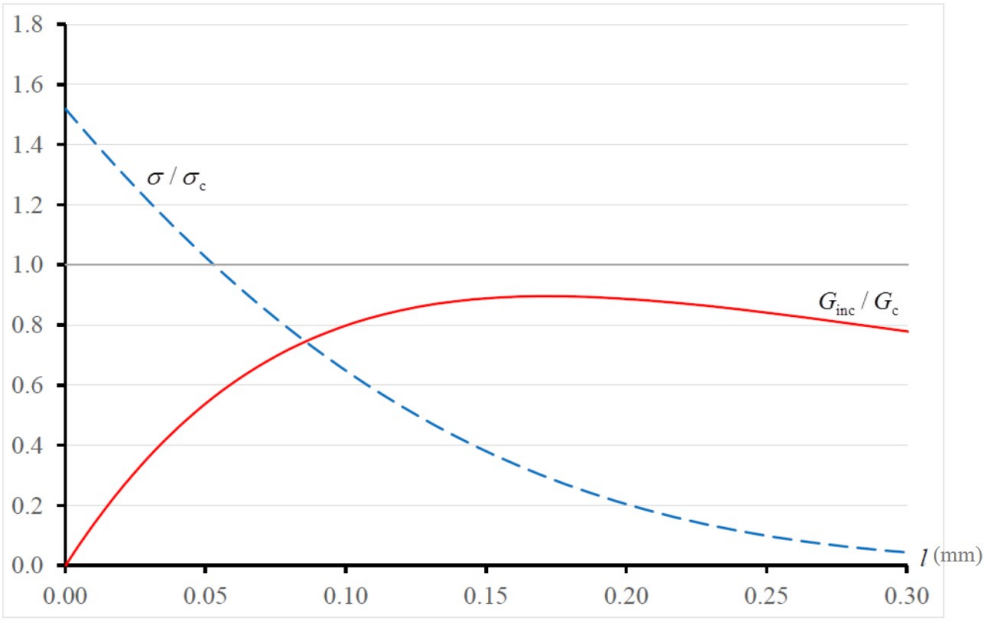

Figure 6: The stress and energy conditions at $t = 1.6$ ms and $\Delta T_0 = 500$ K for $d = 2$ mm. The stress condition is fulfilled for $l \leq 0.06$ mm but the energy condition nowhere.

The actual crack spacing is determined using the method developed in [8, 17, 18]. At a given initiation time t, various decreasing spacings are tested. In each case, the temperature drop likely to cause crack onset is determined based on the CC. It is observed that this temperature drop keeps constant for large spacings and then starts to increase as the crack spacing becomes smaller than a threshold (Figure 11). The actual crack spacing is taken as the smallest spacing prior to the increase in the temperature drop, it corresponds to the maximum dissipation that can be reached at a given temperature drop. According to Figure 11 it is located between 0.8 and 1.4 mm, seemingly independent of the intensity of the thermal shock. It is the order of magnitude found in [13], however, it is obviously difficult to capture accurately the end of the plateau. This may not be very surprising taking into account the large scattering seen in the experiments,

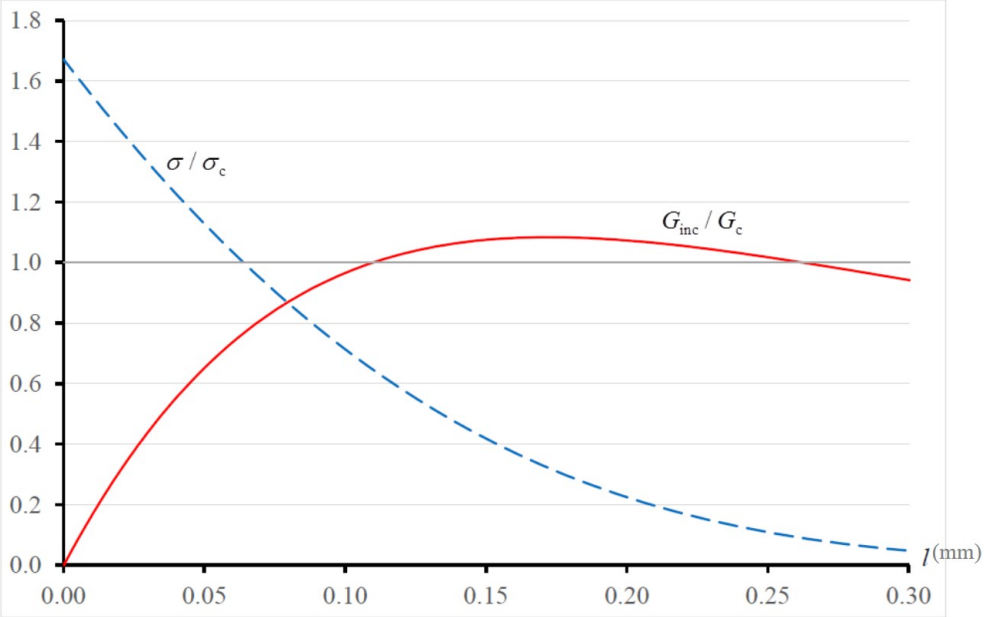

Figure 7: The stress and energy conditions at $t = 1.6$ ms and $\Delta T_0 = 550$ K for $d = 2$ mm. Ranges on which the stress criterion and the energy criterion are disjointed.

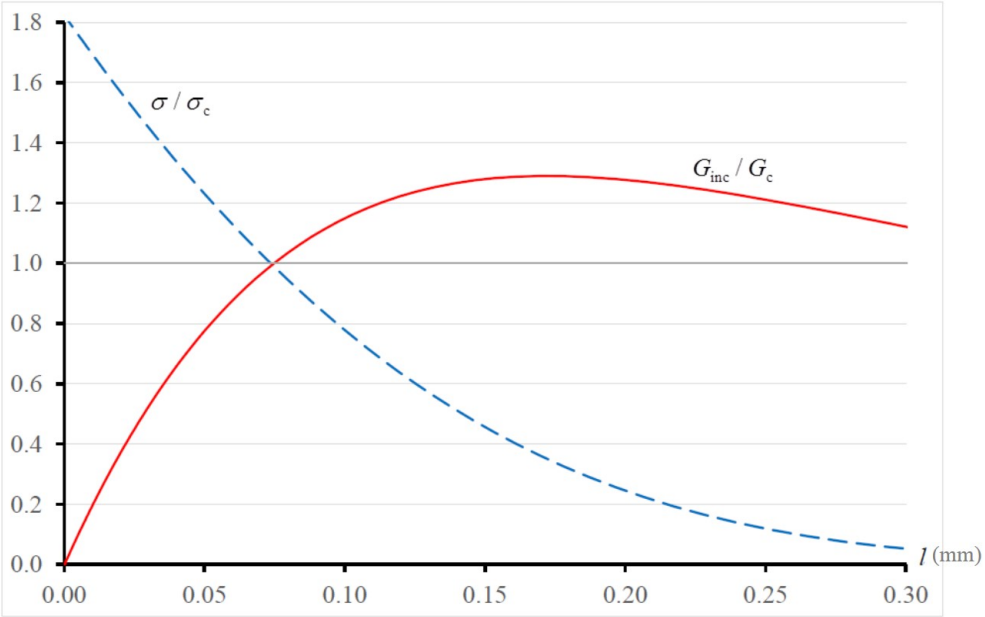

Figure 8: The stress and energy conditions at $t = 1.6$ ms and $\Delta T_0 = 600$ K for $d = 2$ mm. There is crack initiation with $l_c = 0.075$ mm.

spacings of 0.4 mm to 1.6 mm are observed for instance for $\Delta T_0 = 400$ K (see Figure 21 further on). It can be noted that the difficulty to accurately compute the optimal crack spacing is not due to a CC limitation but rather to the plateau beginning determination method itself since the same difficulty was met using the above method with CZM, therefore a different strategy will be proposed in Section 4.3.

To study the crack growth after initiation, the energy release rate G (Eqn. (11)) is superimposed in Figure 12. Then, according to [8, 17, 18], it is clear in figure 12 that following the initiation, the crack grows almost instantaneously in an unstable manner ($G > G_c$). The "arrest length"has two bounds (quotation marks are used because it would be a real

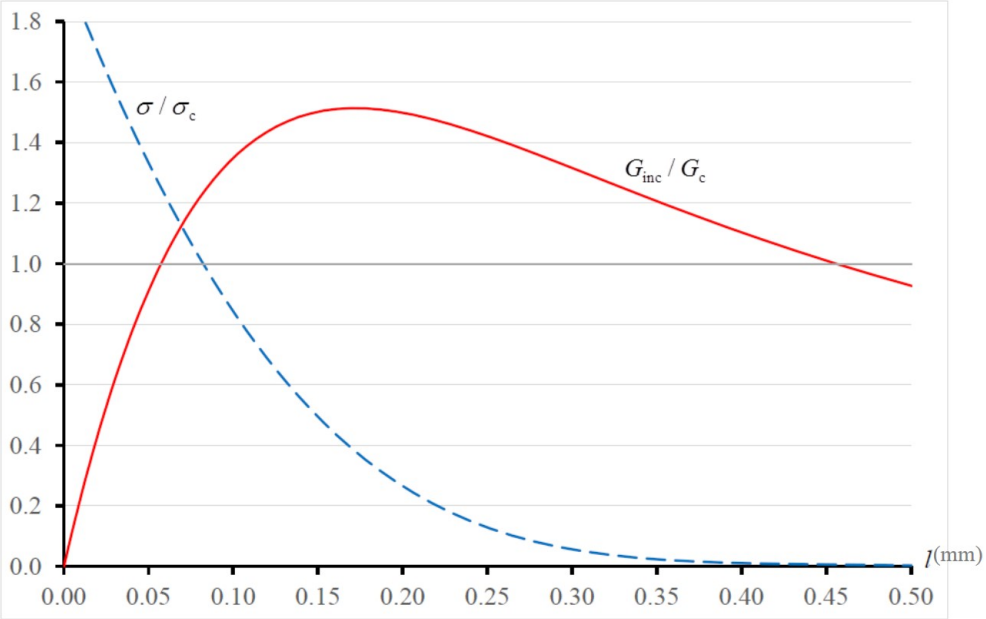

Figure 9: The stress and energy conditions at $t = 1.6$ ms and $\Delta T_0 = 650$ K for $d = 2$ mm. There exists a solution at an earlier time.

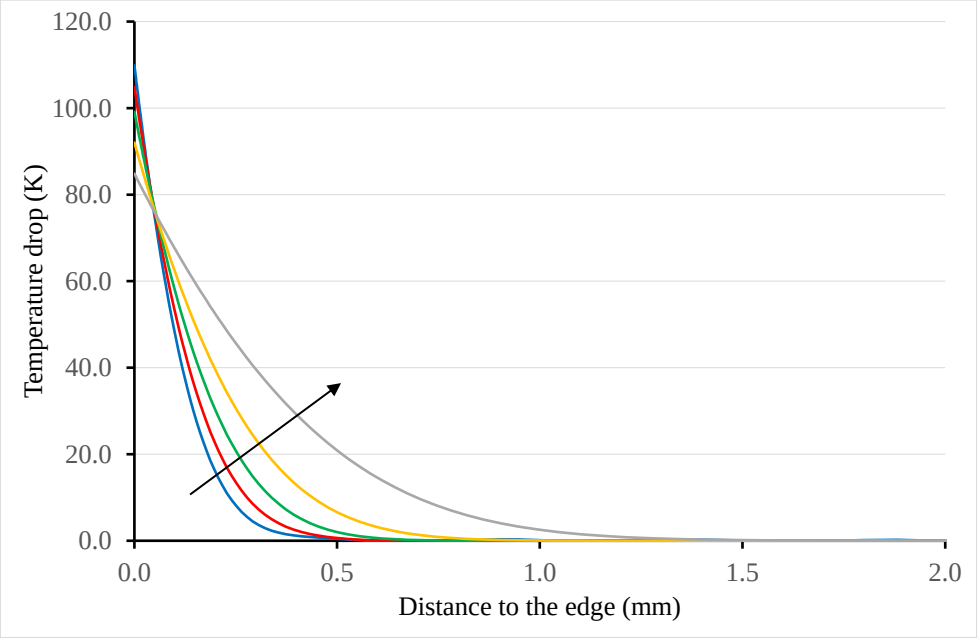

Figure 10: Actual temperature drop $\Delta T = T - T_0$ (as already mentioned, although this is a cooling process, the ΔT values are noted positive) at different times t corresponding to crack nucleation $\Delta T_0 = 600$ K, $t = 1.6$ ms, $\Delta T_0 = 500$ K, $t = 2.2$ ms, $\Delta T_0 = 400$ K, $t = 3.3$ ms, $\Delta T_0 = 300$ K, $t = 5.8$ ms, $\Delta T_0 = 200$ K, $t = 14.8$ ms (following the arrow).

arrest length only if at the same time the cooling mechanism was stopped):
(i) the lower one is defined by $G = G_c$ and $G \searrow$, it is the usual arrest criterion;
(ii) the upper one by $G_{inc} = G_c$ and $G_{inc} \searrow$, the excess energy consequence of the strict inequality $G > G_c$ at initiation

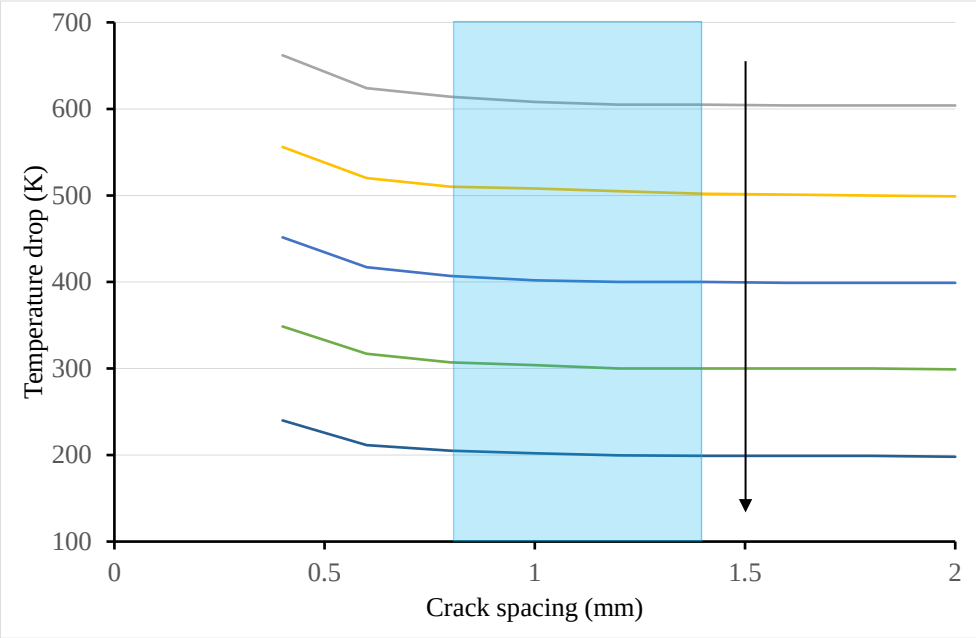

Figure 11: Prescribed temperature drop ΔT_0 triggering crack initiation at $t = 1.6,\ 2.2,\ 3.3,\ 5.8,\ 14.8$ ms (following the arrow), as a function of the crack spacing d. On the right of the shaded area the temperature drop keeps constant, on the left it increases significantly.

being entirely consumed in rupture (refer to [18]).

These bounds, together with the initiation length, are plotted in Figure 13 as functions of the temperature drop ΔT. It should be noted that the experimental measurement of the initiation and arrest lengths is not straightforward since it requires the ability to capture the very moment of crack initiation, for instance using a high-speed camera [27].

In the following, the lower bound will be used, this feature has been observed in many other cases except when the excess energy is extremely large [16].

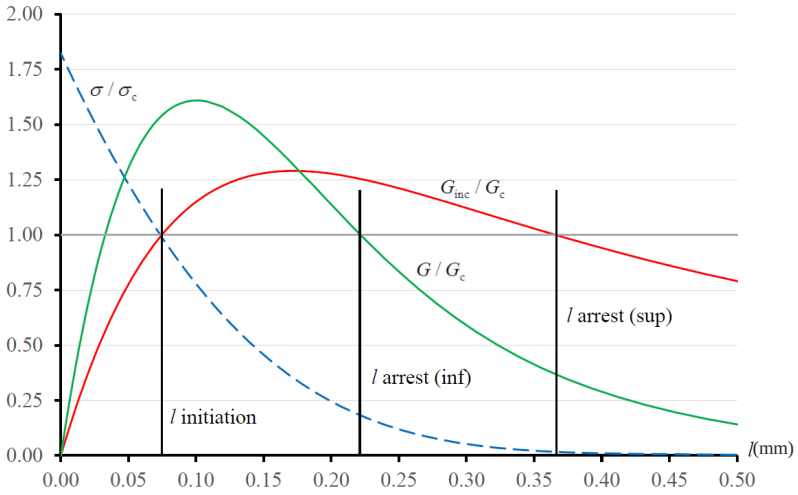

Figure 12: The crack initiation length and the two bounds for the arrest length derived from the CC.

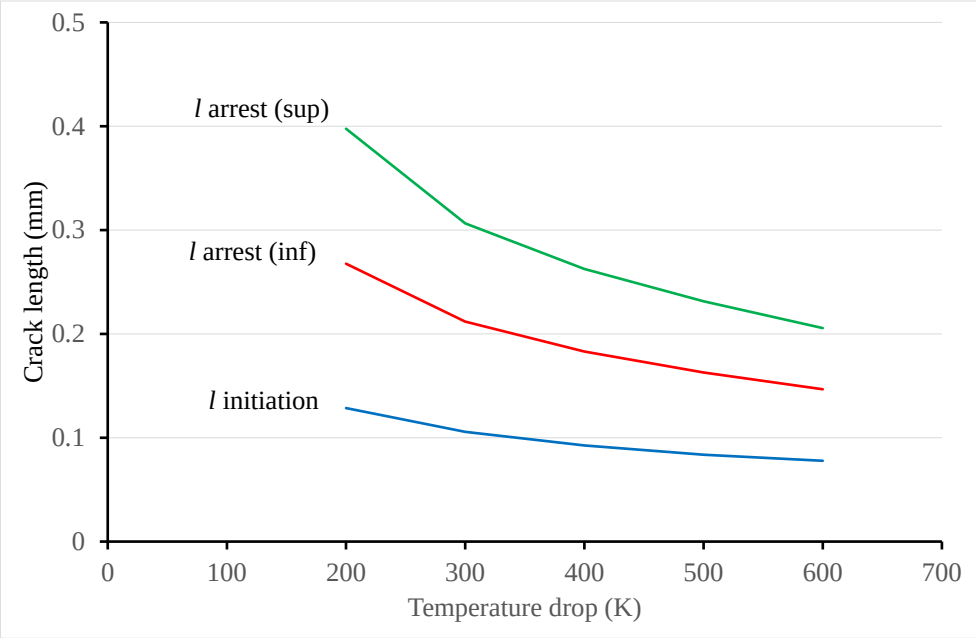

Figure 13: The crack initiation and arrest lengths function of the temperature drop ΔT_0.

ΔT_0 (K)	t (ms)	d (mm)	l init (mm)	l arrest (mm)	Further growth
608	1.75	1	0.075	0.167	Simultaneous growth
502	2.44	1	0.084	0.185	Simultaneous growth
402	3.69	1	0.091	0.213	Transition
304	6.44	1	0.102	0.251	Period doubling
200	16.56	1	0.125	0.323	Period doubling
< 120					No crack initiation

Table 1: Temperature drop, elapsed time at initiation, initiation length, "arrest length"after initiation, further growth. Values differ slightly from those used previously to take into account results presented in Figure 11.

Once initiated and "stopped", the subsequent growth of the crack can be studied using Griffith's criterion. We propose to examine what happens immediately after this first phase, when time continues to elapse, by comparing the growth of the crack in the RVE depicted in Figure 3 (corresponding to the simultaneous growth of all cracks), to the growth of a single crack in the RVE depicted in Figure 5 (corresponding to the growth of one crack out of two, i.e. the doubling of the period). More precisely, twice the energy released by the growth of the crack in case 1 is compared to the energy released by the single crack in case 2 and the most favourable case from the point of view of the energy (i.e. the case leading to the maximum dissipation) is selected [23]. Results are summarized in Table 1. Results of Table 1 are qualitatively in agreement with a comment in [13] stating that the short cracks become shorter as ΔT_0 increased.

4. The cohesive zone model

4.1. The model

A second approach allowing quenching-induced crack initiation and growth to be modeled is cohesive zone modeling (CZM) [4, 10]. Such an approach has already been employed to model cracking in ceramics materials for instance under mechanical [30] or thermal [6] loading. It defines a relation between the cohesive traction T_{n} and the opening displacement δ_{n} of a process zone. As soon as the traction reaches a critical value (taken herein as the material strength), debonding

occurs which triggers a decrease in the cohesive traction (damage) until the opening displacement reaches a critical value δ_c for which the traction becomes null, which corresponds to the nucleation of a crack. The area of the traction-separation profile is the work for separation, *i.e.* G_c for an elastic material with no dissipation effects. For a given traction-separation profile, a relation between G_c, σ_c and δ_c can be straightforwardly derived so that only two of these parameters are required as input. The CZM approach thus requires the same ingredients as for the CC, *i.e.* the material strength σ_c and fracture energy G_c. In addition, the traction separation profile can also be varied. However, all the cohesive zone models are equivalent for studying stable rectilinear crack propagation [1] and the traction-separation profile only has an influence on crack initiation [2, 9] or branching. In the present work, the influence of the traction-separation profile is not studied and a bilinear profile is adopted throughout the analysis (Figure 14).

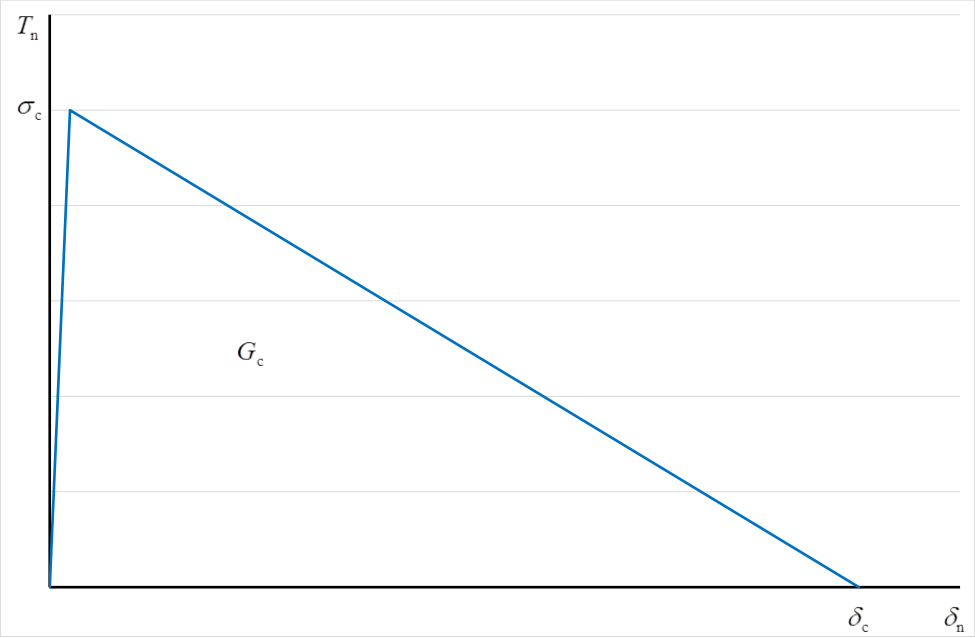

Figure 14: The bilinear cohesive zone model.

4.2. The CZM representative volume element

As above and for analogous reasons, the FE model consists of an infinite specimen modeled by repeating a representative volume element (RVE) with periodic boundary conditions, which is thus representative of the specimen center far for the lateral edges. For practical reasons, the present RVE contains two parallel crack paths on which cohesive zone elements are inserted, which allows modeling initiation of a periodic array of cracks, the simultaneous growth of these cracks as well as the possible subsequent crack period doubling if one out of two cracks stops propagating (Fig. 15).

A material characteristic length defined by $L_{\text{mat}} = \frac{EG_c}{\sigma_c^2}$ allows estimating the process zone extent, which is actually a fraction of this length [29], its value also depending on the prescribed boundary conditions. It was checked that a typical process zone size is around 0.12 mm, which corresponds to 0.44 L_{mat}. The mesh is refined near the cracks so as to ensure that the process zone contains enough elements to well reproduce crack initiation and propagation. The mesh size along the crack path is set to 5×10^{-3} mm.

Symmetry boundary condition $U_y(x, y_0) = 0$ is applied on the top face of the RVE, moreover a displacement $U_x(x_0, y_0) = 0$ at the top left node (see Fig. 15)) is also prescribed to prevent rigid body motions. Periodic boundary conditions are applied to the RVE so as to model an infinite array of cracks. This means that, as in periodic homogenization, the strain field is periodic whereas the traction exerted on the lateral faces are antiperiodic, as a consequence the displacement field

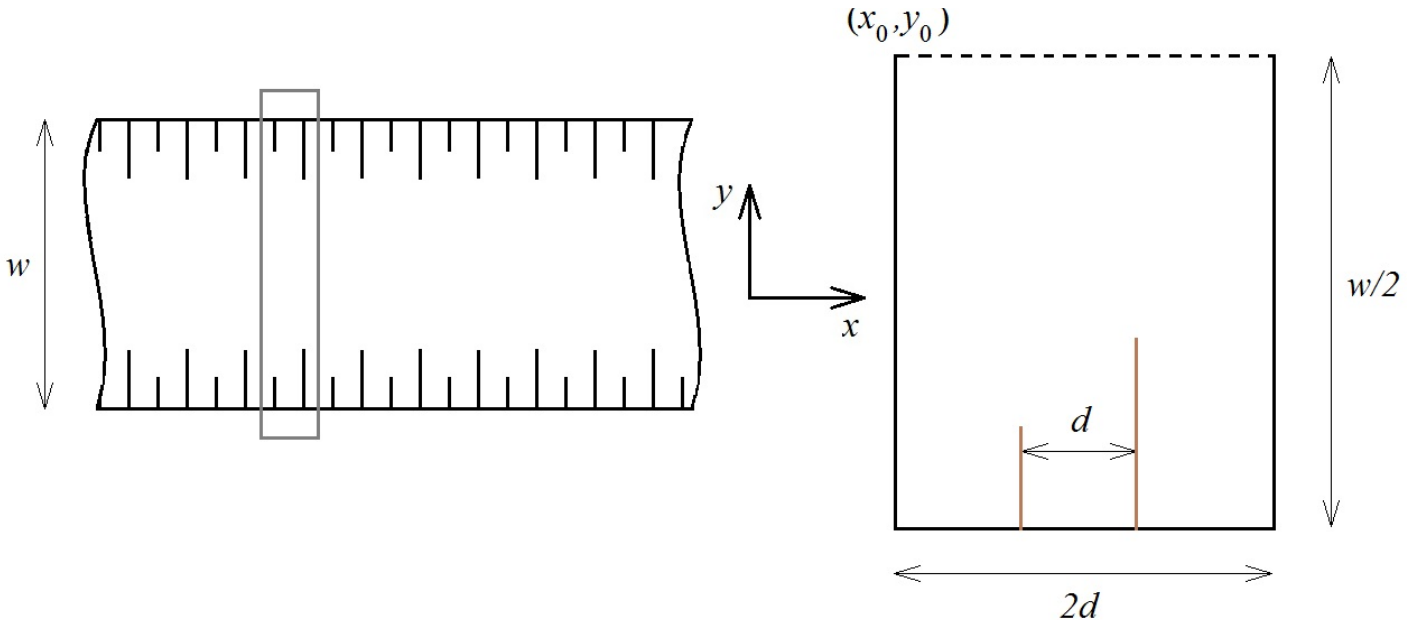

Figure 15: Left: the RVE used with cohesive zones. Right: 1/2 of the RVE, the dashed line is a symmetry axis. Presupposed crack paths where cohesive zone elements are inserted are vertical lines embedding the red solid lines. The red solid lines are an example of cracks after doubling the period.

is the sum of a periodic function and a linear one

$$\begin{array}{l} U_x(x_0+2d,y)-U_x(x_0,y)=2d\ \bar{\varepsilon}_{xx} \\ U_y(x_0+2d,y)-U_y(x_0,y)=2d\ \bar{\varepsilon}_{xy} \end{array} \tag{25}$$

for anypoint (x, y) belonging to the left boundary. Here $\bar{\varepsilon}_{xx}$ and $\bar{\varepsilon}_{xy}$ are the mean strain tensor elongation and shear components (see (14)), which are unknown *a priori* since a thermal loading is applied. However, according to Hooke's law $\sigma_{xy} = 2\mu\varepsilon_{xy}$, then it comes $\bar{\varepsilon}_{xy} = 0$ since $\bar{\sigma}_{xy} = 0$ because (i) no efforts are applied on the lateral faces of the specimen, (ii) the thermal expansion coefficients are isotropic. In addition, according to the condition that prevents rigid body motion, $U_x(x_0 + 2d, y_0) = 2d\bar{\varepsilon}_{xx}$.

To summarize, the boundary conditions can be written (x varies from 0 to $2d$ and y from 0 to $w/2$)

$$\begin{array}{rcl} U_y(x,y_0) & = & 0 \\ U_y(x_0+2d,y) & = & U_y(x_0,y) \\ U_x(x_0,y_0) & = & 0 \\ U_x(x_0+2d,y) & = & U_x(x_0,y)+2d\ \bar{\varepsilon}_{xx} \\ \text{with } \bar{\varepsilon}_{xx} & = & \frac{U_x(x_0+2d,y_0)}{2d} \end{array} \tag{26}$$

Due to the choice of a non-symmetrical RVE, writing boundary conditions is slightly more complicated than in Section 3.2 but the above conditions (26) can be taken into account by most FE codes. In this case, it is essentially the number of cohesive zone elements and the total number of degrees of freedom that determine the cost of the computation.

4.3. Results with CZM

The model presented in Section 4.1 is now applied so as to determine the optimal crack spacing as a function of the temperature drop. Fig. 16 shows the crack length variation as a function of time for the two cracks in the RVE for a temperature drop $\Delta T_0 = 480$ K and a crack spacing $d = 1$ mm. It can be seen that, first, both cracks initiate and propagate simultaneously until reaching a certain length which corresponds to the crack period doubling point, beyond which only one crack out of two propagates while the other one stops. This phenomenon can be explained by the fact that propagating only one crack from this point is a more energetically favourable configuration.
This is not contradictory with results in Table 1 where for such a temperature drop, it is concluded that after initiation

($\Delta T_0 = 500$ K and $l_{\text{arrest}} \simeq 0.185$ mm) there is simultaneous growth of the whole set of cracks, without auguring of further evolution.

We performed simulations with RVE's (Figure 15) containing either one crack (RVE width d) or two cracks (RVE width $2d$) so as to compare models in which the crack period doubling is likely to occur (RVE with two cracks) with a case in which both cracks would continue propagating simultaneously (RVE with one crack). For crack lengths smaller than the one corresponding to the crack period doubling point, the energy of both configurations (i.e. twice the energy in the single crack case) are exactly the same, which is consistent with the simultaneous crack propagation observed prior to the doubling point in Fig. 16. For larger crack lengths, the energy of the configuration with only one out of two cracks propagating is smaller than if both cracks continue propagating (i.e. there is a larger dissipation). Therefore, the former is more energetically favorable than the latter and will be observed in practice.

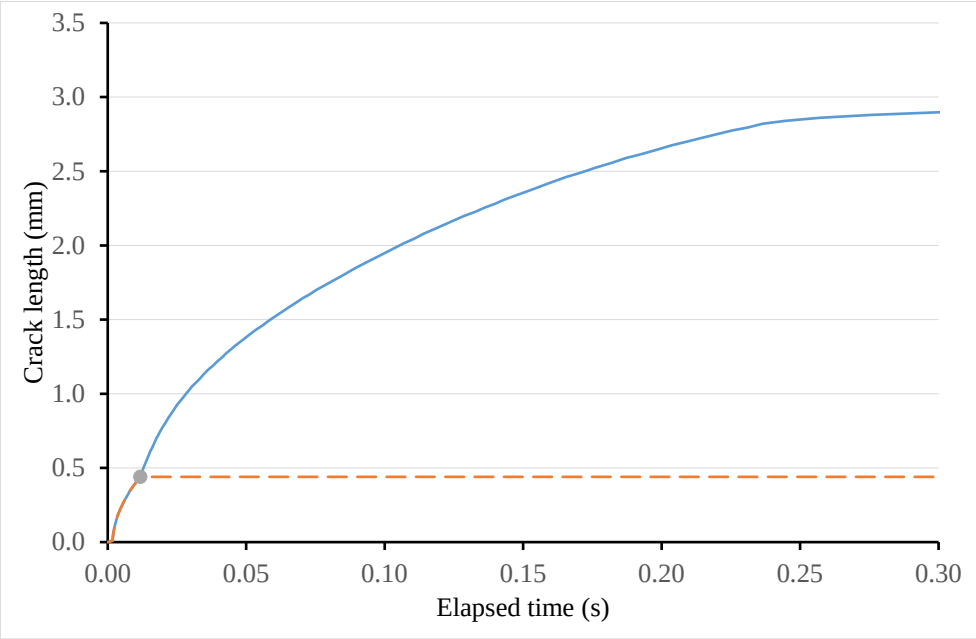

Figure 16: Cracks extensions as a function of time for a RVE containing two cracks.

The crack period doubling point can be determined as a function of the crack spacing for a given temperature drop. Fig. 17 shows the crack length variation as a function of time for several crack spacings for a $\Delta T_0 = 380$ K temperature drop. It can be observed that the smaller the crack spacing, the smaller the time and the length of the crack at the period doubling point.

The crack length at the doubling point as a function of the crack spacing, depicted in Fig. 18, exhibits a linear variation. Therefore, it is possible to determine the minimum spacing d_{opt} for which crack period doubling occurs, which corresponds to the intersection between the line and the abscissa axis. It means that below this value, only one out of two cracks will initiate in the RVE, which finally corresponds to a configuration of a RVE with twice the crack spacing. Therefore, the minimum spacing for which crack period doubling occurs corresponds to the optimal spacing between cracks.

The same procedure has been repeated for several temperature drops. Fig. 19 shows the crack length at the crack period doubling point variation as a function of the crack spacing obtained for temperature drops between 280 and 580 K.

In all cases, a linear variation is obtained which allows determining the optimal crack spacing. The higher the temperature drop, the lower the optimal crack spacing. 20 shows the optimal crack spacing as a function of the temperature drop. A regression of the computed optimal spacings d_{opt} as a function of the temperature drop ΔT_0 has been performed

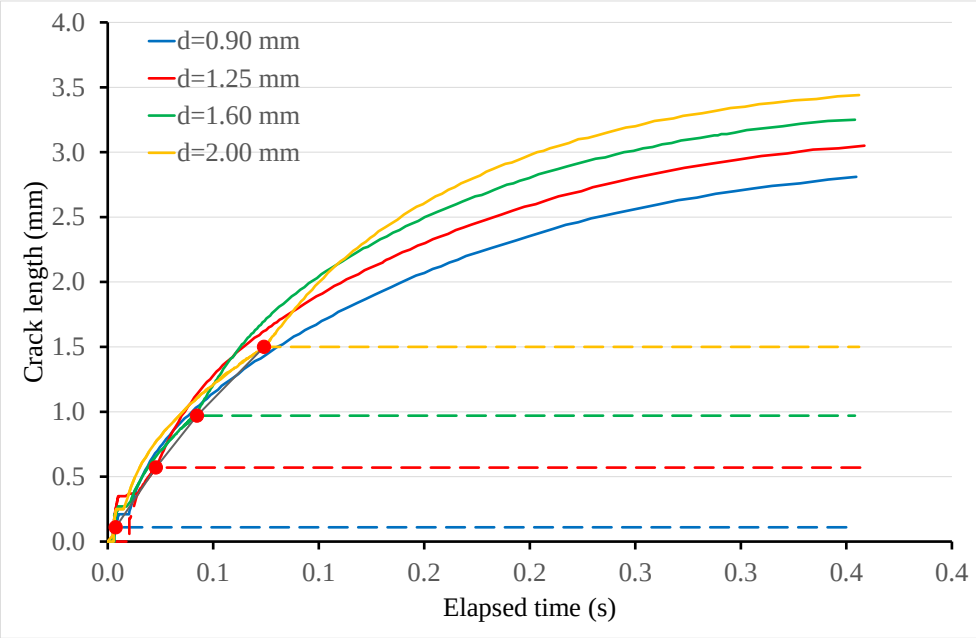

Figure 17: Crack extensions as a function of time for several crack spacings d.

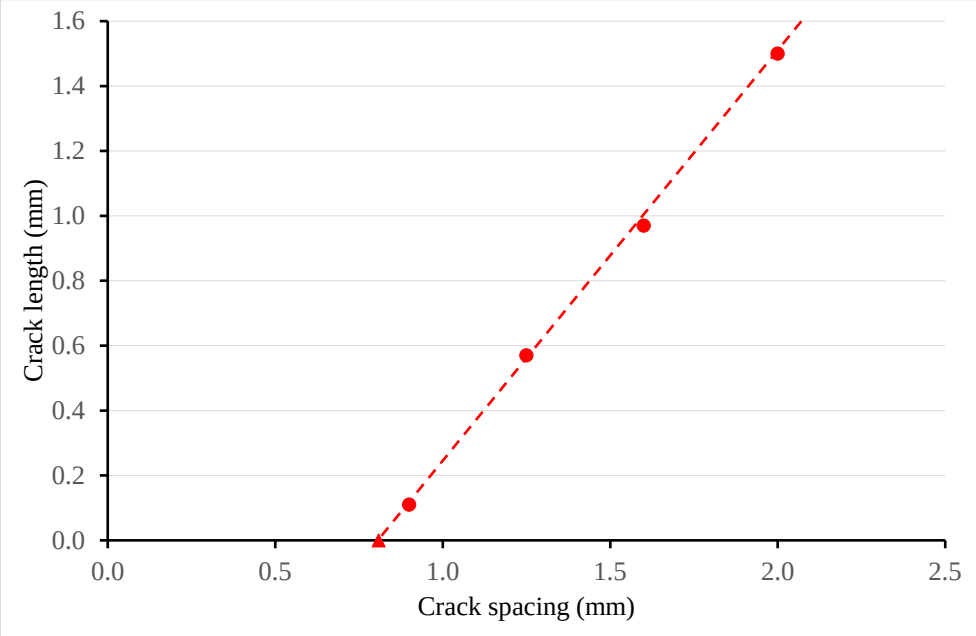

Figure 18: Crack length corresponding to the doubling point as a function of the crack spacing d.

in the form:

$$d_{\text{opt}}(\Delta T_0) = \frac{1}{\sqrt{\frac{\Delta T_0}{\Delta T_{\text{min}}} - 1}} \tag{27}$$

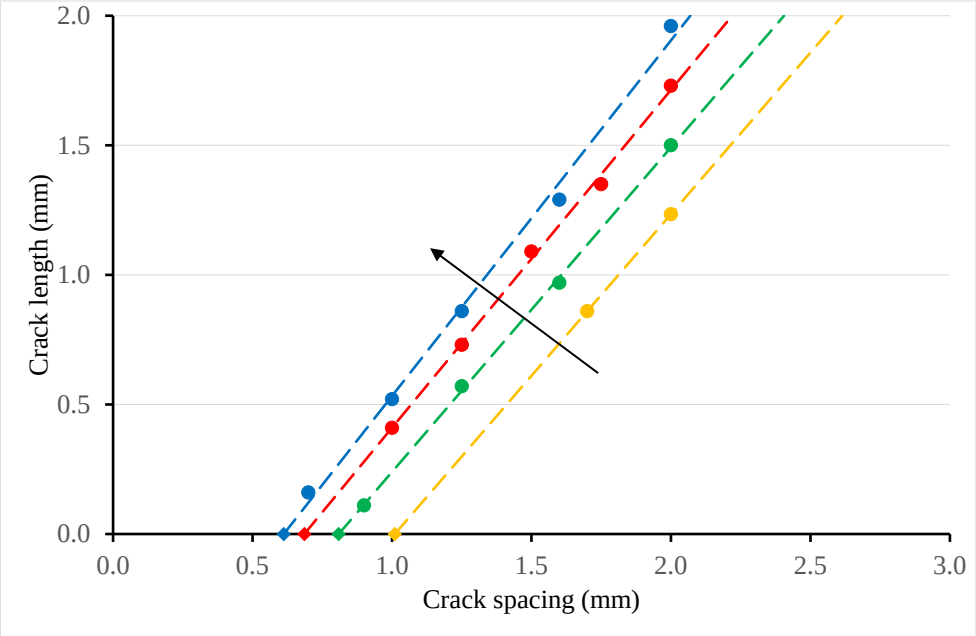

Figure 19: Crack length corresponding to the doubling point as a function of crack spacing obtained for several temperature drops ΔT_0 =280, 380, 480, 580 K following the arrow.

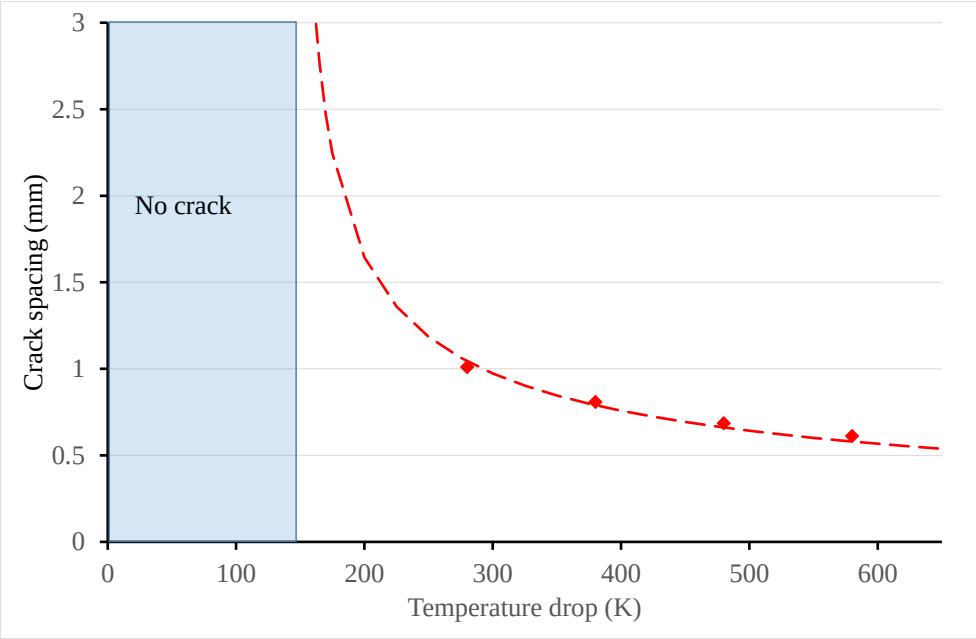

Figure 20: Optimal spacing d_{opt} as a function of the temperature drop.

The chosen regression form has the advantage of involving a single parameter $\Delta T_{\min}$ which has a physical meaning since

it corresponds to the minimum temperature drop below which no cracking occurs during the ceramic quenching. A least-squares fitting of this parameter leads to $\Delta T_{\min}$= 146 K. It can be seen that the chosen function allows a satisfying representation of the optimal spacing variation as a function of the temperature drop and also give access to $\Delta T_{\min}$, which is an essential data for manufacturing ceramic parts that may undergo temperature drops.

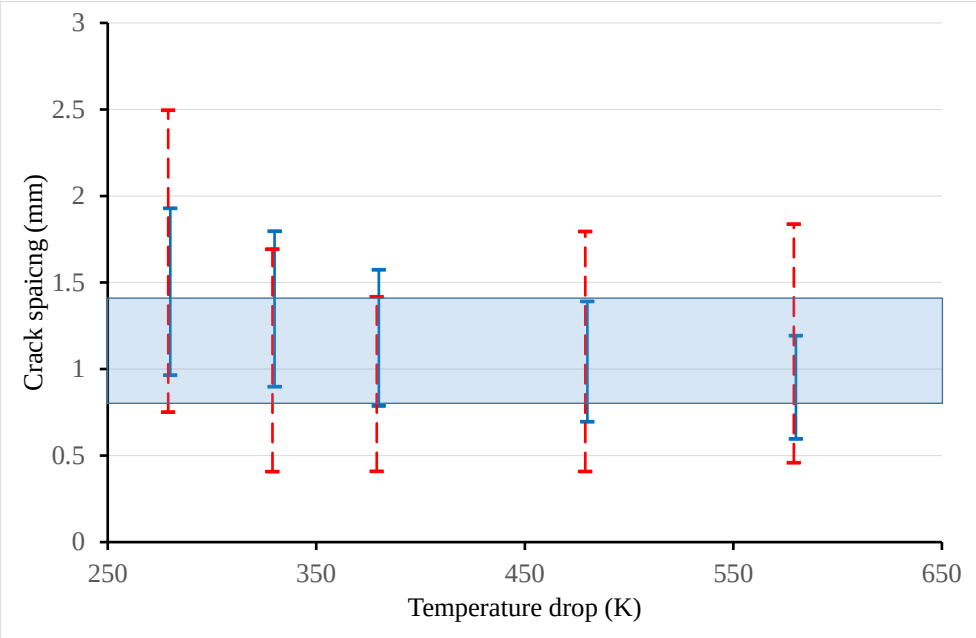

Figure 21: Crack spacing determined experimentally (red dashed line) and numerically (blue solid line) as a function of the temperature drop. Experimental results are taken from [13]. the shaded area corresponds to the bounds determined in Figure 11.

A comparison between the experimental results from [13] and the predictions of the FEM calculations using CZM is displayed in Figure 21. A very large scattering in the crack spacing measured experimentally can be observed. The error bars in the numerical approach correspond to d_{opt} determined by (27) and twice this value. Indeed, we assume that the crack network will subdivide until it falls within this interval for which no further subdivision can occur since d_{opt} is the smallest possible spacing. The shaded area corresponds to the two bounds determined using the CC (see Section 3.3 and Figure 11).

5. Conclusion

The thermal shock induced by a sudden cooling of ceramics results in the nucleation of a set of cracks more or less regularly distributed along the specimen edge. Both CC and CZM allow the determination of the initiation crack length and temperature drop corresponding to a given crack spacing by combining a stress and an energy conditions. Both approaches are complementary, they basically yield similar crack initiation loading and spacing, and their numerical efficiency depends on the searched purpose. A rough estimate of the initial crack spacing can also be obtained by detecting the beginning of a plateau in the temperature drop variation as a function of the crack spacing. However, although it is illusory trying to give a precise spacing so large is the experimental scattering, this method lacks accuracy.

At this stage, the biggest difference lies in the computation time for obtaining the results. The CZM requires solving nonlinear problems which calculation cost depends essentially on the number of nodes located in the cohesive zones. This cost is necessarily high to get a satisfying accuracy. On the contrary, the CC only requests linear resolutions, as many as there are nodes on the presupposed crack path, with a substantial saving in the calculation cost. However, the advantage of the CC stops here, it is only dedicated to the initiation phase, studying the subsequent growth of cracks and the period doubling are beyond its capabilities. This can be done using the Griffith criterion but the prodedure is difficult because it is necessary to consider numerous crack configurations. On the contrary, the same CZM approach can be continued for

analyzing the further crack growth without introducing new complications. This is particularly interesting for investigating in depth the doubling of the period. This cohesive zone approach together with the period doubling made it possible to develop a strategy to determine the initial crack spacing with a higher precision, highlighting a trend in relation to the amplitude of the thermal shock, results are in agreement with the experimental measurements.

References

References

[1] V. Acary, Y. Monerie, 2006. Nonsmooth fracture dynamics using a cohesive zone approach. Research Report RR-6032, INRIA.

[2] G. Alfano, 2006. On the influence of the shape of the interface law on the application of cohesive-zone models. Compos. Sci. Tech 66, 723-730.

[3] H.A. Bahr, H.J. Weiss, U. Bahr, M. Hofmann, G. Fischer, S. Lampenscherf, H.Balke, 2010. Scaling behavior of thermal shock crack patterns and tunneling cracks driven by cooling or drying. J. Mech. Phys. Sol. 58, 1411-1421.

[4] G.I. Barenblatt, 1959. The formation of equilibrium cracks during brittle fracture: general ideas and hypotheses. Axially-symmetric Cracks PMM 23, 622–636.

[5] B. Bourdin, J.J. Marigo, C. Maurini, P. Sicsic, 2014. Morphogenesis and Propagation of Complex Cracks Induced by Thermal Shocks. Phys. Rev. Lett. 112, 014301.

[6] V. Buljak, G. Bruno, 2018. Numerical modeling of thermally induced microcracking in porous ceramics: An approach using cohesive elements. J. Eur. Ceram. Soc. 38(11), 4099-4108.

[7] H.S. Carslaw, J.C. Jaeger, 1959. Conduction of heat in solids (2nd ed.), Oxford University Press.

[8] A. Doitrand, D. Leguillon, 2018. Numerical modeling of the nucleation of facets ahead of a primary crack under mode I+III loading. Int. J. Fract. 213, 37-50.

[9] A. Doitrand, R. Estevez, D. Leguillon, 2019. Comparison between cohesive zone and coupled criterion modeling of crack initiation in rhombus hole specimens under quasi-static compression. Theor. Appl. Fract. Mech. 99, 51-59.

[10] D.S. Dugdale, 1960. Yielding of steel sheets containing slits. J. Mech. Phys. Sol 8,100–104.

[11] D.R. Jenkins, 2005. Optimal spacing and penetration of cracks in a shrinking slab. Phys. Rev. E 71, 056117.

[12] D.R. Jenkins, 2009. Determination of crack spacing and penetration due to shrinkage of a solidifying layer. Int. J. Sol. Struct. 46, 1078-1084.

[13] C.P. Jiang, X.F. Wu, J. Li, F. Song, Y.F. Shao, X.H. Xu, P. Yan, 2012. A study of the mechanism of formation and numerical simulations of crack patterns in ceramics subjected to thermal shock. Acta Mater. 60, 4540-4550.

[14] D. Leguillon, 2002. Strength or toughness? A criterion for crack onset at a notch. Eur. J. of Mech. – A/Sol. 21, 61-72.

[15] D. Leguillon, 2013. A simple model of thermal crack pattern formation using the coupled criterion. C. R. Mécanique 341, 538-546.

[16] D. Leguillon, E. Martin, O. Seveček, R. Bermejo, 2015. Application of the coupled stress-energy criterion to predict the fracture behaviour of layered ceramics designed with internal compressive stresses. Eur. J. Mech. A/Sol., 54, 94-104.

[17] D. Leguillon, J. Li, E. Martin, 2017. Multi-cracking in brittle thin layers and coatings using a FFM model. Eur. J. Mech. A/Sol. 63, 14-21.

[18] D. Leguillon, E. Martin, 2018. Prediction of multi-cracking in sub-micron films using the coupled criterion. Int. J. Fract. 209(1), 187-202.

[19] D. Leguillon, E. Martin, O. Seveček, R. Bermejo, 2018. What is the tensile strength of a ceramic to be used in numerical models for predicting crack initiation? Int. J. Fract. 212(1), 89-103.

[20] Y.N. Li, A.E. Hong and Z.P. Bazant, 1995. Initiation of parallel cracks from surface of elastic half-plane. Int. J. Fract. 69, 357-369.

[21] J. Li, F. Song, C. Jiang, 2013. Direct numerical simulations on crack formation in ceramic materials under thermal shock by using a non-local fracture model. J. Eur. Ceram. Soc. 33, 2677-2687.

[22] E. Martin, D. Leguillon, O. Seveček, R. Bermejo, 2018. Understanding the tensile strength of ceramics in the presence of small critical aws, Engng Fract. Mech. 201, 167-175.

[23] Q.S. Nguyen, C. Stolz, G. Debruyne, 1990. Energy methods in fracture mechanics: stability, bifurcation and second variations. Eur. J. Mech. A/Sol. 9, 157-173.

[24] K. Park, G.H. Paulino, 2011. Cohesive Zone Models: A critical review of traction-separation relationships across fracture surfaces. Appl. Mech. Rev. 64(6): 060802. (20 pages)

[25] Y. Shao, X. Xu,S. Meng, G. Bai, C.Jiang, F. Song, 2010. Crack Patterns in Ceramic Plates after Quenching. J. Am. Ceram. Soc. 93, 3006-3008.

[26] Y. Shao, Y. Zhang, X. Xu, Z. Zhou, W. Li, B. Liu, 2011. Effect of Crack Pattern on the Residual Strength of Ceramics After Quenching. J. Am. Ceram. Soc. 94, 2804-2807.

[27] Y. Shao, F. Song, B. Liu, W. Li, L. Li, C. Jiang. Observation of ceramic cracking during quenching. J Am Ceram Soc 2016; 100: 520-523.

[28] P. Sicsic, J.J. Marigo, C. Maurini, 2017. Initiation of a periodic array of cracks in the thermal shock problem: A gradient damage modeling. J. Mech. Phys. Sol. 63, 256-284.

[29] A. Turon, C.G. Dávila, P.P. Camanho, J. Costa, 2007. An engineering solution for mesh size effects in the simulation of delamination using cohesive zone models. Engng. Fract. Mech. 74, 1665-1682.

[30] R. Vargas, J. Neggers, R.B. Canto, J.A.Rodrigues, F. Hild, 2019. Analysis of a castable refractory using the wedge splitting test and cohesive zone model. J. Eur. Ceram. Soc. 39(13), 3903-3914.

[31] P. Weissgraeber, D. Leguillon D., W. Becker, 2016. A review of Finite Fracture Mechanics: Crack initiation at singular and non-singular stress-raisers. Arch. Appl. Mech. 86, 375-401.

[32] X. Wu, C. Jiang, F. Song, J. Li, Y. Shao, X. Xu, P. Yan, 2015. Size effect of thermal shock crack patterns in ceramics andnumerical predictions. J. Eur. Ceram. Soc. 35, 1263-1271.